

Polarized electron-beam acceleration driven by vortex laser pulses

Yitong Wu,^{1,2} Liangliang Ji,^{1,3} Xuesong Geng,¹ Qin Yu,¹ Nengwen Wang,¹ Bo Feng,¹ Zhao Guo,¹ Weiqing Wang,¹ Chengyu Qin,¹ Xue Yan,¹ Lingang Zhang,¹ Johannes Thomas,⁵ Anna Hützen,^{6,7} Markus Büscher,^{6,7} Peter Rakitzis,^{8,9} Alexander Pukhov,⁵ Baifei Shen,^{1,3,4} and Ruxin Li^{1,3,10}

¹State Key Laboratory of High Field Laser Physics, Shanghai Institute of Optics and Fine Mechanics, Chinese Academy of Sciences, Shanghai 201800, China

²Center of Materials Science and Optoelectronics Engineering, University of Chinese Academy of Sciences, Beijing 100049, China

³CAS Center for Excellence in Ultra-intense Laser Science, Shanghai 201800, China

⁴Shanghai Normal University, Shanghai 200234, China

⁵Institut fuer Theoretische Physik I, Universitaet Duesseldorf, 40225 Germany

⁶Peter Grünberg Institut (PGI-6), Forschungszentrum Jülich, Wilhelm-Johnen-Str. 1, 52425 Jülich, Germany

⁷Institut für Laser- und Plasmaphysik, Heinrich-Heine-Universität Düsseldorf, Universitätsstr. 1, 40225 Düsseldorf, Germany

⁸Department of Physics, University of Crete, 71003 Heraklion-Crete, Greece

⁹Institute of Electronic Structure and Laser, Foundation for Research and Technology-Hellas, 71110, Heraklion-Crete, Greece

¹⁰Shanghai Tech University, Shanghai 201210, China

E-mail: jill@siom.ac.cn and ruxinli@mail.shcnc.ac.cn

Abstract

We propose a new approach based on an all-optical set-up for generating relativistic polarized electron beams via vortex Laguerre-Gaussian (LG) laser-driven wakefield acceleration. Using a pre-polarized gas target, we find that the topology of the vortex wakefield resolves the depolarization issue of the injected electrons. In full three-dimensional particle-in-cell simulations, incorporating the spin dynamics via the Thomas-Bargmann Michel Telegdi equation, the LG laser preserves the electron spin polarization by more than 80% at high beam charge and flux. The method releases the limit on beam flux for polarized electron acceleration and promises more than an order of magnitude boost in peak flux, as compared to Gaussian beams. These results suggest a promising table-top method to produce energetic polarized electron beams.

Keywords: Polarized electron beams, laser wakefield acceleration, Laguerre-Gaussian laser, particle-in-cell simulation

1. Introduction

Spin is an intrinsic form of angular momentum carried by elementary particles [1]. Numerous studies in particle physics and material science have been carried out using spin-polarized electron beams [2], including tests of the Standard Model [3], studies of parity violation [4], probing nuclear structure [5], exploring molecular dynamics [6] as well as the generation of polarized photons [2,7] and positrons [2,8]. Generally, there are two approaches to generate polarized electron beams. One mostly used is to extract polarized electrons from polarized atoms and photo-cathodes [2,9,10], or through spin [11] and beam filters [12], with subsequent acceleration in linear accelerators. The other approach relies on radiative self-polarization (the Sokolov-Ternov effect) [2,13] in storage rings. Both methods involve accelerators that are typically very large in scale and budget [2], and suffer from limitations on the beam flux due to the restrictions of the operational voltage [14,15].

Compared to conventional accelerators, laser-driven wakefield acceleration (LWFA) has the potential to generate energetic electron beams in a more compact and cost-efficient approach. However, for the realization of a laser-driven accelerator for polarized electron beams several challenges need to be addressed: i) Since a significant build-up of electron polarization from an initially unpolarized target during laser acceleration does not happen [16,17], it requires the use of a gas target where the electron spins are already aligned before laser irradiation. ii) Polarization losses during the injection of as many as possible electrons into a bubble structure and iii) subsequent acceleration in the wake field must be kept under control and minimized.

With regard to polarized electron targets suitable for LWFA we have witnessed promising developments in recent years. Electron spin polarization in strong-field ionization of atoms has been widely studied both theoretically [18-23] and experimentally [18-20]. Gas targets with spin polarization $\sim 40\%$ have been achieved using near-infrared light [18-20]. It is also predicted that the polarization can reach 90% by adapting ultraviolet (UV) light [19,20]. The most promising approach seems to be a technique employing the UV photodissociation of hydrogen halides [16,24,25], reaching gas densities of approx. 10^{19}cm^{-3} at high polarization of the electrons in the hydrogen and halogen atoms [26-28](See detail in Section 2).

The perspective of all-optical laser-driven polarized electron acceleration therefore relies on addressing the key issues ii) and iii), i.e., electron depolarization during LWFA. As shown below, spin depolarization mainly happens in the injection phase, which is in line with previous studies [29]. This can be mitigated by fine tuning the focal position of the Gaussian laser beam [30]. Here we propose a new scheme that resolves the key challenge on beam depolarization in LWFA. We utilize the topology of electron beams driven by vortex laser pulses and demonstrate in full three-dimensional particle-in-cell simulations the generation of high polarization electrons at very high beam charge and peak flux. Such laser beams are readily accessible, for example, with the Laguerre Gaussian (LG) mode [31,32].

The paper is organized as follows: In Section 2 we give descriptions of a promising approach to generate polarized electron target and parameters setup for simulations. In Section 3 we present the results of simulations and analysis. In Section 4 we give discussions for different stating spin directions. Finally in Section 5, we give a brief summary.

2. Scheme descriptions and Simulation Setup

As stated above, preparation a pre-polarized electron target is crucial to our scheme. Known from

previous literatures, the photodissociation of hydrogen halides with circularly polarized UV light yields highly spin-polarized hydrogen and halogen atoms [26,27], at gas densities of at least 10^{19} cm^{-3} [28]. The polarization can approach 100% for specific photodissociation wavelengths (for HCl this is near 213 nm), and if the molecular bonds are aligned prior to photodissociation [24]; otherwise, if the bonds are isotropic, the polarization is reduced to 40%. However, the electronic polarization of the halogen atoms is very low; specifically, the core electrons are completely unpolarized. Therefore, to maximize the polarization of all accelerated electrons, the halogen atoms can be ionized with a resonant laser (e.g. via 2+1 resonance-enhanced multiphoton ionization (REMPI), for Cl atoms at 234.62 nm [26]) and removed from the target volume with either electric fields before irradiation by the accelerating laser pulse.

With this in mind, the all-optical scheme is sketched in Fig.1. A spin-polarized hydrogen-atom target is prepared [16] from the photodissociation of HCl gas emitted from a nozzle, using circularly polarized UV light, so that the electron spins are oriented along the UV-laser propagation direction. This is followed by the driving vortex LG pulse with a well-controlled time synchronization. The latter, propagating coaxially with the UV light, stimulates a plasma wakefield in the gas target and accelerates pre-polarized electrons to high energies.

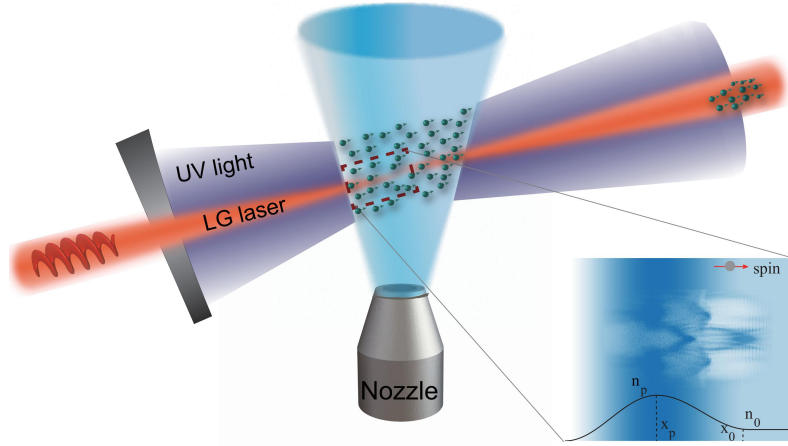


FIG. 1. Sketch of the all-optical laser-driven polarized electron acceleration scheme. UV light with a wavelength of 213 nm is used to photo-dissociate HCl molecules, thereby producing polarized electrons in the gas target. The density profile of the gas target and LG-driven bubble is shown in the lower-right. For the sake of simplicity we do not show two optional laser beams (1064 nm IR laser to align the bonds of the HCl molecules, 234.62 nm UV laser to ionize the Cl atoms) and the electric field for removal of the Cl atoms from the target volume prior to irradiation by the accelerating laser pulse. A coaxial LG laser pulse traverses the gas target to accelerate the polarized electrons via wakefield acceleration.

The main influence during wakefield acceleration on the spin evolution is its precession in electric and magnetic fields according to the Thomas-Bargmann-Michel-Telegdi (T-BMT) equation, where gradient forces can be neglected [33]. Other mechanisms like the Sokolov-Ternov effect (spin-flip) and the Stern-Gerlach effect are negligibly small thus have been omitted here [16,17,34]. Electron spin dynamics is therefore integrated into the PIC simulation code VLPL [35] based on the T-BMT equation [36]:

$$ds/dt = (\mathbf{\Omega}_T + \mathbf{\Omega}_a) \times \mathbf{s} \quad (1)$$

with $\Omega_T = \frac{e}{m} \left(\frac{\mathbf{B}}{\gamma} - \frac{1}{\gamma+1} \frac{\mathbf{v}}{c^2} \times \mathbf{E} \right)$ the normal precession frequency and $\Omega_a = a_e \frac{e}{m} \left(\mathbf{B} - \frac{\gamma}{\gamma+1} \frac{\mathbf{v}}{c^2} (\mathbf{v} \cdot \mathbf{B}) - \frac{\mathbf{v}}{c^2} \times \mathbf{E} \right)$ the anomalous one proportion to $a_e = (g-2)/2 \approx 1.16 \times 10^{-3}$ (g is the gyromagnetic factor). The

vector $\mathbf{s} = \langle \boldsymbol{\varphi} | \boldsymbol{\sigma} | \boldsymbol{\varphi} \rangle$ with $|\mathbf{s}|=1$ describes the electron spin following Ehrenfest's theorem, where $\boldsymbol{\varphi}$ denotes the normalized two-component spinor and $\boldsymbol{\sigma}$ the Pauli matrices [2]. Here m and $-e$ represent the mass and charge, \mathbf{v} denotes the velocity and $\gamma = 1/(1-v^2/c^2)^{-1/2}$ is the relativistic factor, respectively.

The LG laser propagates along the x axis from left side of simulations window of $48\mu\text{m}(x) \times 48\mu\text{m}(y) \times 48\mu\text{m}(z)$ in size and $1200 \times 600 \times 600$ in cell numbers, and passes through the fully ionized cold plasma. We employ the LG₀₁ mode laser [37-39]:

$$E(r,t) = E_0 \frac{\sqrt{2r}}{w^2(x)} \exp\left[-\frac{r^2}{w^2(x)}\right] \sin^2\left(\frac{\pi t}{2\tau}\right) \exp\left\{-i\left[2 \tan^{-1}\left(\frac{x}{x_R}\right) - \phi - \frac{k_0 r^2 x}{2(x^2 + x_R^2)}\right]\right\} \quad (2)$$

with $r^2 = y^2 + z^2$, $\phi = \arctan(z/y)$, wavelength $\lambda = 800\text{nm}$, $k_0 = 2\pi/\lambda$, $w(z) = w_0 \{[(x-x_f)^2 + x_R^2]/x_R^2\}^{1/2}$, $x_R = \pi w_0^2/\lambda$ and the focusing position x_f , respectively. The laser pulse is linearly polarized along the y axis. For comparison, we also give results for a Gaussian laser with the same parameters. In our set-up, the gas density is tailored to form a density ramp for efficient electron injection [40-42] with following profile: (I) $2x_p - x_0 < x < x_p$, $n(x) = n_p \{1 + \cos[\pi(x_p - x)/(x_0 - x_p)]\}/2$, (II) $x_p < x < x_0$, $n(x) = (n_p - n_0) \{1 + \cos[\pi(x_p - x)/(x_0 - x_p)]\}/2 + n_0$, (III) $x > x_0$, $n(x) = n_0$. Here $n_p = 4 \times 10^{18} \text{cm}^{-3}$, $n_0 = 10^{18} \text{cm}^{-3}$ are the densities at the peak ($x_p = 36\mu\text{m}$) and plateau (from $x_0 = 52\mu\text{m}$), respectively. Initially all the electrons have spin directions along the $+x$ axis which means $\mathbf{P} = \sum_i^N \mathbf{s}_i / N = \mathbf{P}_x = 1$.

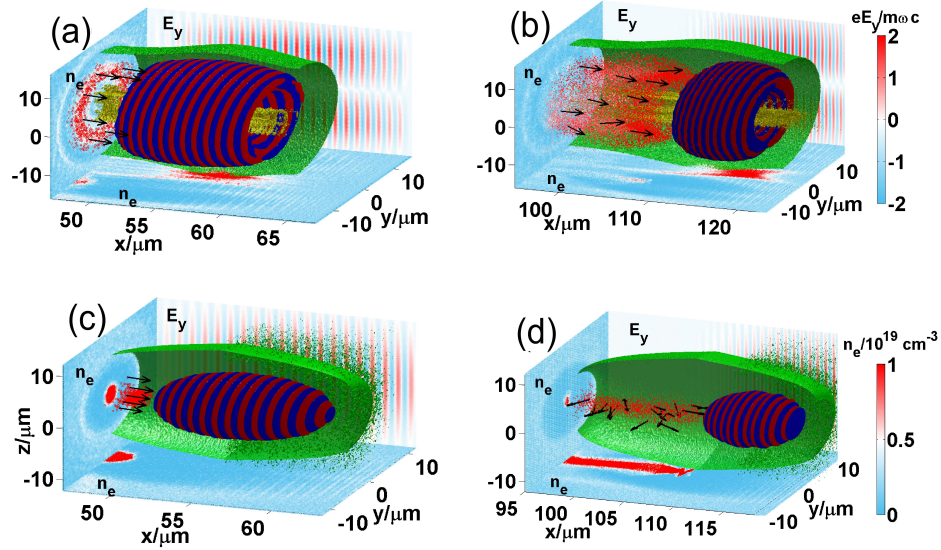


FIG. 2. Electron density and laser field distributions (iso-surface) with $a = eE_y/m\omega c = 2$ and $x_f = 250\lambda$ for the LG laser at (a) $75T_0$, (b) $150T_0$ and the Gaussian laser (c) $75T_0$ and (d) $150T_0$. The black arrows denote the electron spin directions. Both lasers are of beam radius $w_0 = 12.5\lambda$ and pulse duration $\tau = 8T_0$ (T_0 is the laser period).

3. Results and theoretical analysis

The acceleration processes in both cases are illustrated in Fig. 2, at the same peak intensity of $8.6 \times 10^{18} \text{W/cm}^2$ and pulse duration of 21.4 fs. The ordinary Gaussian beam drives a bubble wakefield that traps local electrons due to the decreasing phase velocity in the plasma density bump [43]. A cylindrical electron bunch is formed in the bubble center, as depicted in Fig. 2(c) and (d). The spins of the injected electrons are well aligned in the same direction at $75T_0$. However, at a later stage of $150T_0$

the spin orientations are strongly diverged at different positions. Averaging the spin projections onto the propagation axis, one finds that the overall polarization is vanishing, i.e., the electron beam is depolarized.

The LG laser, however, introduces a different topology to the bubble structure, due to its unique transverse intensity profile [44,45]. Electrons are no longer injected near the axis as they are for the Gaussian beam. Instead, they clusterize off axis in the donut-shaped bubble where the laser intensity peaks and get injected as a ring bunch, cf. Fig. 2(a). Remarkably, these injected electrons preserve their spin orientation (arrows pointing in x direction). The beam is of high polarization due to the new structure brought by the vortex laser driver.

We then track all the electrons trapped in the bubble and calculate the beam polarization and the average relativistic factor $\langle\gamma\rangle$ at each interaction time. As illustrated in Fig. 3(a), the polarization decreases significantly at the early stage with $\langle\gamma\rangle$ varying slowly. This is followed by steady acceleration of electrons where the polarization is almost constant. The former, corresponding to the injection phase of LWFA, is when the major depolarization happens. Along the simulation, one finds that the polarization is maintained at a very high level ($>80\%$) for the LG case, while the one for the Gaussian beam is almost zero. This fact is further illustrated from the evolution of the spin distribution in Fig. 3(b). The spins dilute between -1 and 1 for the Gaussian laser, while most trapped electrons accumulate at unity for the LG laser.

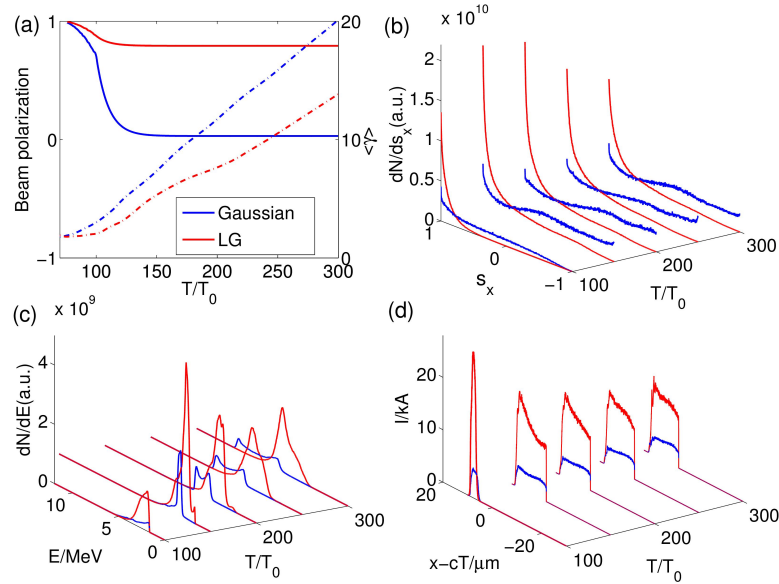


FIG.3. Results for trapped electrons located in bubble wake. Displayed are the evolution for (a) polarization (solid lines) and electron relativistic factor $\langle\gamma\rangle$ (averaged, dashed lines), (b) the s_x distribution, (c) energy spectrum and (d) electric current. Red and blue colors represent the LG and Gaussian laser beams.

From the energy spectrum in Fig. 3(c) and the electric current in Fig. 3(d) we see that, while the cutoff and peak energies are marginally smaller for the LG case, the total number of electrons is significantly higher than that for the Gaussian beam. This generates an enormous electron-beam flux. For instance, the peak current of the LG case reaches 20 kA (polarization $>80\%$), about 4 times larger than in the Gaussian case (5 kA, polarization $<1\%$), as illustrated in Fig. 3(d). The boosted bunch charge or the peak flux benefits from the new geometry of the LG-laser-driven wakefield. The vortex beam produces a donut-shaped electron bunch in the vicinity of $r_0 \pm \Delta r/2$, as compared to a cylinder-like

beam of radius Δr for the Gaussian driver, corresponding to a cross-section area of $2\pi r_0 \Delta r$ and $\pi \Delta r^2$, respectively. For a simple estimation, we use $\Delta r \sim a^{1/2} \lambda_p(x_p) / \pi \sim 4 \mu\text{m}$ [30,44,46] as the bunch radius of the trapped electrons and $r_0 = w_0 / \sqrt{2} \approx 7 \mu\text{m}$ as the center of the trapped region for the LG case [44]. Accordingly, the peak-current ratio between the LG and the Gaussian case is about $2r_0 / \Delta r \sim 3.5$, a factor that is well reproduced in simulations.

The disparity between the two driving laser beams stems from the different electron spin dynamics in LWFA. Since $\langle \gamma \rangle$ remains of the order of unity during injection, the precession frequency for electron spin can take the non-relativistic limit of Eq.(1), implying $\Omega \approx \Omega_T \approx eB_\phi / m$ where B_ϕ is the azimuthal magnetic field. Considering the symmetry of the B_ϕ distribution [30,44,46], the transverse polarization $\langle \mathbf{P}_y \rangle \approx \langle \mathbf{P}_z \rangle \approx 0$ and $\mathbf{P} \approx \mathbf{P}_x = \sum_i s_x / N$, with s_x the spin projection onto the x -axis. It should be mentioned that in LWFA, electrons experience spin oscillations when interacting with the laser pulse. But the oscillations are symmetric such that the spin polarization returns to its original state after passing through the laser pulse (see Section 4).

We average B_ϕ over the trapped electron region and display its values in the y - z plane during injection in Fig.4. For the LG case (Fig. 4(a)), B_ϕ is anticlockwise in the near axis region ($-5 \mu\text{m} < r < 5 \mu\text{m}$), decays to zero as the radius increases, and changes to clockwise in the outer region. Differently, the B_ϕ field for the Gaussian laser is clockwise in the whole displayed area and gradually declines (Fig. 4(c)). One sees that the peak magnetic field in the former is less than half of that in the latter. As a matter of fact, the azimuthal magnetic field B_ϕ in the cavity satisfies [43,44]:

$$B_\phi(r) = \frac{1}{r} \int_0^r \left(\frac{J_x}{\epsilon_0 c^2} - \frac{\partial E_x}{\partial x} \right) r' dr' \quad (3)$$

We assume $\partial E_x / \partial r \sim 0$ since in the blowout regime of LWFA the longitudinal electric field is slowly varying in the trapping area. Therefore, the field strength depends on two quantities: the longitudinal current density (J_x) and the electric field (E_x) along the x axis. Since it is known for the blow-out regime that $|j_x / \epsilon_0 c^2| / |\partial E_x / \partial x| \sim n_p / n_0 \gg 1$ [46-48], the difference is mainly due to the self-generated magnetic field of the beam current.

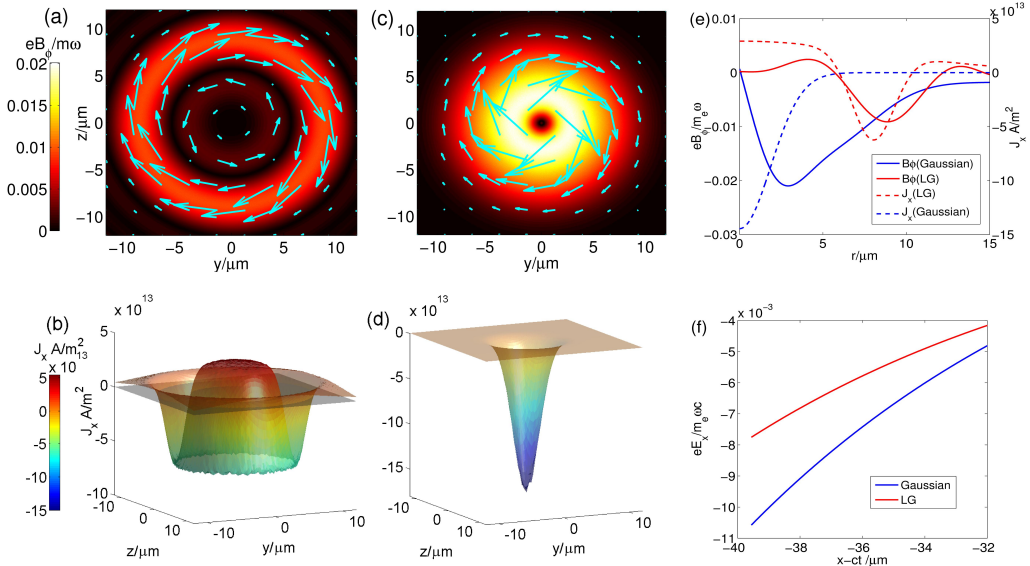


FIG.4. Color-map of the averaged azimuthal magnetic field B_ϕ (a) and current density along x direction J_x (b) during injection in the trapping region in the y - z plane for LG case (a) & (b) and for the Gaussian case (c) and (d). Blue arrows show the direction and amplitude of the averaged B_ϕ . Averaged B_ϕ and J_x as a function of the radius r (e) and the longitudinal electric field E_x as a function of $x-ct$ (f).

For a Gaussian laser, the light intensity peaks on-axis such that trapped electrons are concentrated at the center of the bubble, leading to a well-directed current in the counter-propagation direction, as shown in Fig. 4(d). One finds the highest field strength near the symmetry axis. On the contrary, the intensity of the LG laser beam is maximized off-axis, leaving a hollow space in the propagation center. Two consequences immediately arise: First, trapped electrons are distributed in a circular ring with their density peaking at around $r = 7 \mu\text{m}$. The new topology significantly lowers down the electron areal density and the current density for certain amount of beam charge. Second, electrons located near the symmetry axis leak through the beam center and become the source of a counter-propagating return flux in the region of $r < 5 \mu\text{m}$. These effects lead to the unique current density profile for the LG driver in Fig. 4(b), where the peak current density in the trapping region is only one-third of that for a Gaussian beam. The already weakened magnetic field is further effectively compensated by the anti-clockwise field resulting from the return current. Together, they strongly reduce B_ϕ while maintaining the total beam charge or flux, as lined out along the radial distance in Fig. 4(e). We also note that the longitudinal accelerating field E_x , linearly dependent on the phase [46-48], is notably smaller in the LG case as seen from Fig. 4(f). It leads to less acceleration compared to the Gaussian case (Fig. 3(c)). A possible explanation is that the residual electron density within the cavern is larger compared to the Gaussian case due to the donut-shaped vortex distribution, which weakens E_x formed by the background ions.

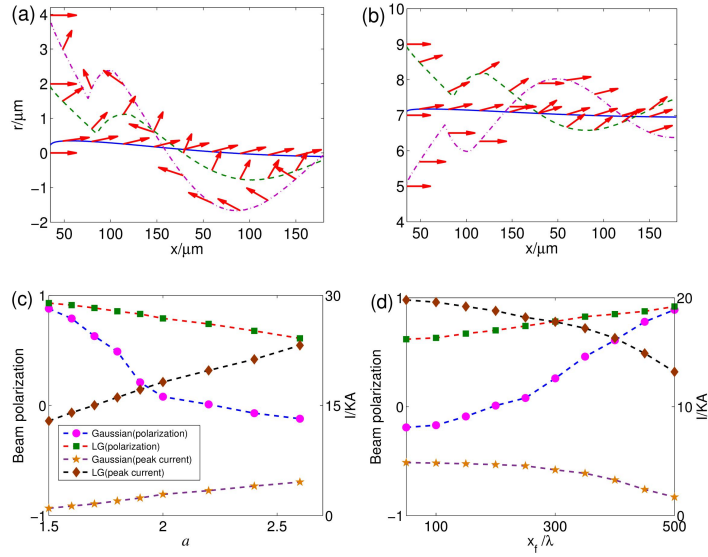


FIG.5. The orbits with spin directions (red arrows) of (a) the Gaussian and (b) the LG case for trapped electrons at different injection radii. Blue solid, green dashed and pink dash-dotted lines represent injection positions $0, \Delta r/2, \Delta r$ for the Gaussian case and $r_0, r_0 + \Delta r/2, r_0 - \Delta r/2$ for the LG case respectively. Polarization and peak current for different parameters at $300T_0$ (800fs): (c) Peak amplitude a in the range 1.5–2.6 with focus position at 250λ and (d) focus position at 50 – 500λ with fixed peak amplitude $a=2$.

The essence of beam depolarization is that electron spins precess at difference frequencies. Eventually the unsynchronized spins are oriented in various directions such that the averaged spin, i.e., the beam polarization, vanishes. A direct observation of the depolarization process will be tracking the specific electrons during injection and acceleration. We chose three electrons for each case, at injection radii of $0, \Delta r/2, \Delta r$ for the Gaussian laser and $r_0, r_0 + \Delta r/2, r_0 - \Delta r/2$ for the LG laser, and present the orbits with spin directions in Fig. 5(a) and (b). The azimuthal magnetic fields experienced by the electrons at

each instance are shown in Fig. 5(a) and (b). In the Gaussian case, the electron spins oscillate at much higher frequencies due to larger B_ϕ (see Fig.4) and lose their initial spin orientations almost instantly; they even flip for $r = \Delta r$. The electron beam is of course depolarized. As already analyzed, the field is so much weaker for the LG case that the spin evolves much slower and their directions for off-axis electrons remain well-aligned along the propagation axis (Fig. 5(b)).

Recalling that $\Omega \approx eB_\phi/m$ during the injection phase and taking the limit of slowly varying frequency $|d\Omega/dt| \ll |\Omega|^2$, the spin precession can be approximated by an oscillating function $s_x \approx \cos(e \langle B_\phi \rangle \Delta t/m)$ at frequencies depending on the averaged magnetic field $\langle B_\phi \rangle$. Electrons located at different transverse locations see a B_ϕ of varying strength and their spins precess differently. One obtains the beam polarization via averaging the changes of the spin orientations in the trapping area, i.e., $P \approx \int_{r_0 - \Delta r/2}^{r_0 + \Delta r/2} \cos(e \langle B_\phi(r) \rangle \Delta t/m) r dr / r_0 \Delta r$ for the LG case and $P \approx \int_0^{\Delta r} \cos(e \langle B_\phi(r) \rangle \Delta t/m) 2r dr / \Delta r^2$ for the Gaussian case. We ignore the radial variation and assume a homogeneous density distribution here. During the injection time estimated by $\Delta t \approx 4a^{1/2} \lambda_p / \pi c \approx 74 T_0$ [30,49,50] (see also Fig. 4(a)), we calculate a polarization of about 0.84 for the LG case and 0.11 for the Gaussian case from the B_ϕ profiles in Fig. 4(e), in good agreement with the simulation results from Fig. 5(a).

After electrons gaining sufficiently high energies the spin directions remain almost unchanged ($t > 150T_0$), although B_ϕ alters dramatically due to the oscillations along the transverse direction. Solving the T-BMT equation for a relativistic electron, one acquires $\Delta\theta_s \approx \Omega \Delta t$ where $\Delta\theta_s$ is the rotation angle of spin s . In steady acceleration, one has $E_r \sim cB_\phi, v \sim v_x = \beta_x c$ [41] (see also Fig.4) which indicates $|\Omega_a / \Omega_T| \sim a_e \ll 1$ for $\beta_x \approx 1$ and $\gamma \gg 1$. Therefore the precession frequency can be written as $\Omega \approx \Omega_T \approx eB_\phi/m\gamma(\gamma+1)$, suggesting the electron spin precession is slowed down due to $\gamma \gg 1$. Substituting the equation of motion for electrons $\gamma/\Delta t \sim d\gamma/dt \sim eE_x/mc$ into the precession frequency, we finally obtain $\Delta\theta_s \sim cB_\phi/E_x(\gamma+1) \sim 1/\gamma \ll 1$, i.e., the spin change is negligible during the acceleration phase.

Spin depolarization imposes strong restrictions on the charge or the current of the electron beam from LWFA. One can find out the criteria for the Gaussian laser beam by taking $B_\phi \sim B_0 r / \Delta r \sim \pi e n_p r / 2\epsilon_0 c$ [51,52] and the radius of the injection volume $\Delta r = (I_{peak} / \pi e n_p c)^{1/2}$. The polarization is obtained from the statistic average of spins in the injection volume:

$$P = \frac{\int_0^{\Delta r} s_x 2r dr}{\Delta r^2} = \frac{2 \left[\cos(\sqrt{kI_{peak}}) + \sqrt{kI_{peak}} \sin(\sqrt{kI_{peak}}) - 1 \right]}{kI_{peak}} \quad (4)$$

where $k = \pi e^3 n_p \Delta t^2 / 4m^2 \epsilon_0^2 c^2$. Hence to retain polarization $> 80\%$, the restriction $I_{peak} < 2.6 \text{ kA}$ applies. In Fig.5(c) and (d) we show systematic scans at various laser amplitudes a and focal positions. In all cases the beam current is limited to $I_{peak} < 2.2 \text{ kA}$ for the Gaussian laser to preserve polarizations over 80%, consistent with the prediction in Eq. (4). However, the limitation on the beam flux is released because of the vortex beam structure. The peak current for the LG case I_{peak} reaches 21.2kA where the polarization is $> 80\%$, an order of magnitudes higher.

4. Discussion

As we mentioned in Section 3, electrons preserve their spin after passing through the laser. To prove this, we choose three trapped electrons at different injection positions and plot the s_x evolution when electrons are interacting with the laser pulse depicted in Fig.6(a) and (b). The

electrons experience spin oscillations during this stage and P_x (polarization on x axis) reduces at the first half cycle while increase to the initial value(~ 1) in the later cycle, which indicates the electrons do not gain net change of the spin orientations. Due to the symmetrical oscillations of the laser field, the spin polarization returns to its original state after the passage of the laser pulse. Therefore, we only consider the spin precession after the beginning of injection.

Our simulations are carried out for initial electron polarization along the laser propagation (x) axis. Nevertheless, our scenario is valid for all starting spin directions, in particular for transversally polarized electron beams. We carried out simulations of $s_x=1$ (parallel to propagation direction) and $s_y=1$ (perpendicular to propagation direction) at the beginning for both the LG and Gaussian case, and the corresponding spin component distributions are illustrated in Fig.6(c) and (d). In the latter, the spin precession frequency is proportional to $\mathbf{B}_\perp = \mathbf{B}_x + \mathbf{B}_\phi \times \mathbf{s}$, dependent on both B_x and B_ϕ . For electrons trapped in LWFA $v_x \sim c$ [44,46], so that $J_x \gg J_\phi$ and $B_x \ll B_\phi$ [43]. Therefore, B_ϕ still plays the dominate role in the spin precession. Since the precession frequency can be almost zero in some directions (for example, $\mathbf{B}_\phi \parallel \mathbf{s}$), the beam polarization is preserved at an even higher degree than that of the longitudinal polarization. The beam polarization of the LG driven case reaches 88.6% for traverse polarization($s_y=1$), higher than 81.2% for longitudinal polarization($s_x=1$). For the Gaussian case, polarization is 14% and 4%, respectively, and is thus still larger for traverse-polarized electrons. However in that case, the design in Fig. 1 has to be modified by aligning the UV beam perpendicular to the driving LG laser.

In fact, a simple expression can be given for the traverse-polarized case. Taking $\Omega \approx eB_\phi \sin\theta/m$, here $\sin\theta = |\mathbf{B}_\phi \times \mathbf{s}|/|B_\phi|$, one obtains the beam polarization via averaging the changes of the spin orientations in the trapping area, i.e., $P \approx \int_0^\pi \int_{r_0-\Delta r/2}^{r_0+\Delta r/2} \cos\left(e \langle B_\phi(r) \rangle \sin\theta \Delta t/m\right) r dr d\theta / \pi r_0 \Delta r$ for the LG case and $P \approx \int_0^\pi \int_0^{\Delta r} \cos\left(e \langle B_\phi(r) \rangle \sin\theta \Delta t/m\right) 2r dr d\theta / \pi \Delta r^2$ for the Gaussian case. Compared to the longitudinally polarized results in our manuscript, the polarization is clearly larger.

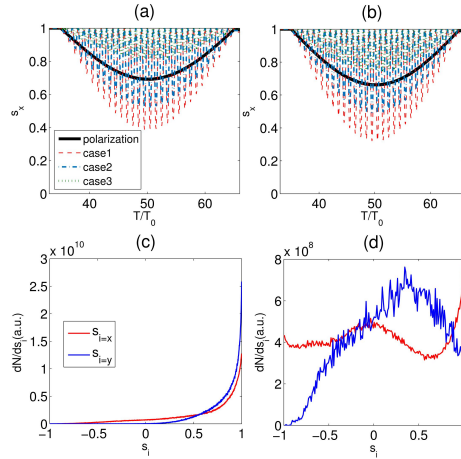


Fig.6. The evolution of s_x for three track electrons and polarization on x axis for LG(a) and Gaussian(b) case. The black solid lines denote the polarization, while red dash lines, blue dotted dash lines, and green dotted lines represent results injection positions at $0, \Delta r/2, \Delta r$ for the Gaussian case, and $r_0, r_0+\Delta r/2, r_0-\Delta r/2$ for the LG case, respectively. The Spin component distribution at $300T_0$ ($T_0 = \lambda/c = 2.67$ fs is the laser cycle) for LG(c) and Gaussian(d) case. The red lines denote s_x distribution for $s_x=1$ at initially (parallel to propagation direction) while blue lines for s_y distribution for $s_y=1$ at initially(perpendicular to propagation direction).

5. Conclusions

In conclusion, we proposed a promising scheme to generate polarized electron beams via LWFA driven by a vortex Laguerre-Gaussian Laser. According to our 3D-PIC simulations involving particle spin dynamics, electron beam is of polarization over 80% is achieved with high beam charge and peak flux. Compared to the Gaussian laser driven acceleration, the restriction on the electron beam current density is released, thanks to the novel topology of the vortex LG laser. The scheme relies on an all optical set-up that is accessible at state-of-the-art facilities.

Acknowledgements

We acknowledge Prof. Andreas Lehrach for helpful discussions. This work is supported by the Strategic Priority Research Program of Chinese Academy of Sciences (Grant No. XDB 16010000), the National Science Foundation of China (No. 11875307) and the Recruitment Program for Young Professionals. The German authors acknowledge support through the HGF-ATHENA project.

References

- [1]. E. Merzbacher. Quantum mechanics. Phys. Today 24(6):49- 50(1970).
- [2]. S. R. Mane, Y. M. Shatunov, and K. Yokoya. Spin-polarized charged particle beams in high-energy accelerators. Rep. Prog. Phys. 68(9):1997-2265(2005).
- [3]. Androic, D. et al(The Jefferson Lab Qweak Collaboration). Precision measurement of the weak charge of the proton. Nature 557(7704):207-211(2018).
- [4]. B. S. Schlimme et al. Measurement of the neutron electric to magnetic form factor ratio at $Q^2 = 1.58 \text{ GeV}^2$ using the reaction $3\text{He}(e,e'n)\text{pp}$. Phys. Rev. Lett.111(13):132504 (2013).
- [5]. E. S. Ageev et al(COMPASS Collaboration). Measurement of the spin structure of the deuteron in the DIS region [rapid communication]. Phys. Lett. B 612(3-4):154-164(2005).
- [6]. T. J. Gay. Advances In Adv. Atom. Mol. Opt. Phys. Vol. 57,pp. 157 – 247(2009)(Academic Press, New York).
- [7]. R. Märtin, G. Weber, R. Barday, Y. Fritzsche, U. Spillmann, W. Chen, R. D. DuBois, J. Enders, M. Hegewald, S. Hess, A. Surzhykov, D. B. Thorn, S. Trotsenko, M. Wagner, D. F. A. Winters, V. A. Yerokhin, and Th. Stöhlker. Polarization transfer of bremsstrahlung arising from spin-polarized electrons. Phys. Rev. Lett. 108(26):264801(2012).
- [8]. D. Abbott et al(PEPPo Collaboration). Production of Highly Polarized Positrons Using Polarized Electrons at MeV Energies. Phys. Rev. Lett. 116(21):214801(2016).
- [9]. J. Kessler. Polarized Electrons. Springer Berlin Heidelberg (1985).
- [10]. D. T. Pierce, F. Meier, and P. Zurcher. Negative electron affinity GaAs: A new source of spin-polarized electrons. Appl. Phys. Lett. 26(12):670-672(1975).
- [11]. H. Batelaan, A. S. Green, B. A. Hitt, and T. J. Gay. Optically Pumped Electron Spin Filter. Phys. Rev. Lett. 82(21):4216-4219(1999).
- [12]. M. M. Dellweg, and C. Müller. Spin-Polarizing Interferometric Beam Splitter for Free Electrons. Phys. Rev. Lett. 118(7):070 403(2017).
- [13]. A. A. Sokolov, and I. M. Ternov. Synchrotron radiation. Soviet Phys. J. 24(2):47-47 (1971).
- [14]. J. Maxson, I. Bazarov, B. Dunham, J. Dobbins, X. Liu, and K. Smolenski. Design, conditioning, and performance of a high voltage, high brightness dc photoelectron gun with variable gap. Rev. Sci. Instrum. 85(9):69(2014).
- [15]. C. Sun, J. Zhang, J. Li, W. Z. Wua, S. F. Mikhailov, V. G. Popov, H. L. Xu, A. W. Chao, and Y. K. Wu.

Polarization measurement of stored electron beam using Touschek lifetime. *Nucl. Instrum. Meth. B* 614(3):339-344(2010).

[16]. A. Hützen, J. Thomas, J. Böker, R. Engels, R. Gebel, A. Lehrach, A. Pukhov, T. P. Rakitzis, D. Sofikitis, and M. Büscher. Polarized Proton Beams from Laser-induced Plasmas. *High Power Laser Sci.* in print, DOI: 10.1017/hpl.2018.73.

[17]. J. Thomas, A. Hützen, A. Lehrach, A. Pukhov, and M. Büscher. “Spin-polarized ion beams from a plasma accelerator” , publication in preparation for *Phys. Rev. Accel. Beams*.

[18]. A. Hartung, F. Morales, M. Kunitski, K. Henrichs, A. Laucke, M. Richter, T. Jahnke, A. Kalinin, M. Schöffler, L. P. H. Schmidt, M. Ivanov, O. Smirnova, and R. Dörner. Electron spin polarization in strong-field ionization of Xenon atoms. *Nat. Photonics* 10(8)(2016).

[19]. Ming-Ming Liu, Yun Shao, Meng Han, Peipei Ge, Yongkai Deng, Chengyin Wu, Qihuang Gong, and Yunquan Liu. Energy and Momentum-Resolved Photoelectron Spin Polarization in Multiphoton Ionization of Xe by Circularly Polarized Fields. *Phys. Rev. Lett.* 120(4):043201(2018).

[20]. D. Trabert, A. Hartung, S. Eckart, F. Trinter, A. Kalinin, M. Schöffler, L. Ph. H. Schmidt, T. Jahnke, M. Kunitski, and R. Dörner. The role of spin and angular momentum in strong-field ionization. *Phys. Rev. Lett.* 120(4):043202(2018).

[21]. K. Liu and I. Barth. Nonadiabatic tunnel ionization of current-carrying orbitals of prealigned linear molecules in strong circularly polarized laser fields. *Phys. Rev. A* 94(4):043402(2016).

[22]. K. Liu, K. Renziehausen and I. Barth. Producing spin-polarized photoelectrons by using the momentum gate in strong-field ionization experiments. *Phys. Rev. A.* 95(6): 063410(2017).

[23]. D. Ayuso, A. J. Galán, F. Morales, M. Ivanov, and O. Smirnova. Attosecond control of spin polarization in electron-ion recollision driven by intense tailored fields. *New J. Phys.* 19(7):073007(2017).

[24]. D. Sofikitis, P. Glodic, G.Koumariou, H. Jiang, L. Bougas, P. C. Samartzis, A. Andreev, and T. P. Rakitzis. Highly Nuclear-Spin-Polarized Deuterium Atoms from the UV Photodissociation of Deuterium Iodide. *Phys. Rev. Lett.* 118, 233401 (2017).

[25]. D. Sofikitis, L.Rubio-Lago, L. Bougas, A. J. Alexander, and T. P. Rakitzis. Laser detection of spin-polarized hydrogen from HCl and HBr photodissociation: Comparison of H- and halogen-atom polarizations. *J. Chem. Phys.* 129, 144302 (2008).

[26]. T. P. Rakitzis, P. C. Samartzis, R. L. Toomes, T. N. Kitsopoulos, Alex Brown⁴, G. G. Balint-Kurti, O. S. Vasylutinskii, and J. A. Beswick. Spin Polarized Hydrogen Atoms from Molecular Photodissociation. *Science*, 300, 1936 (2003).

[27]. T. P. Rakitzis. Pulsed-Laser Production and Detection of Spin-Polarized Hydrogen Atoms. *A European Journal of Chemical Physics & Physical Chemistry*, 5, 1489 (2004).

[28]. Dimitris Sofikitis, Chrysovalantis S. Kannis, Gregoris K. Boulogiannis, and T. Peter Rakitzis. Ultrahigh-density spin-polarized H and D observed via magnetization quantum beats. *Phys. Rev. Lett.* 121, 083001 (2018).

[29]. J. Vieira, C.-K. Huang, W. B. Mori, and L. O. Silva. Polarized beam conditioning in plasma based acceleration. *Phys. Rev. Accel. and Beams* 14, 071303(2011).

[30]. M. Wen, M. Tamburini, and C. H. Keitel. Polarized laser-wakefield-accelerated kiloampere electron beams. *arXiv:1809. 10570* (2018).

[31]. J. Vieira, R. M. G. M. Trines, E. P. Alves, R. A. Fonseca, J. T. Mendonça, R. Bingham, P. Norreys, and L. O. Silva. Amplification and generation of ultra-intense twisted laser pulses via stimulated Raman scattering. *Nat. Commun.* 7(3):10371(2016).

[32]. Yin Shi, Baifei Shen, Lingang Zhang, Xiaomei Zhang, Wenpeng Wang, and Zhizhan Xu. Light fan driven by

- relativistic laser pulse. *Phys. Rev. Lett.* 112(23):235001(2014).
- [33]. R. H. Good. Classical Equations of Motion for a Polarized Particle in an Electromagnetic Field. *Phys. Rev.* 125, 2112 (1962).
- [34]. M. Wen, C. H. Keitel, and H. Bauke. Spin-one-half particles in strong electromagnetic fields: Spin effects and radiation reaction. *Phys. Rev. A* 95, 042102 (2017).
- [35]. A. Pukhov. Three-dimensional electromagnetic relativistic particle-in-cell code VLPL (Virtual Laser Plasma Lab). *J. Plasma Phys.* 61(3):425-433 (1999).
- [36]. V. Bargmann, L. Michel, and A. V. L. Telegdi. Precession of the polarization of particles moving in a homogeneous electromagnetic field. *Special Relativity and Quantum Theory* (1988).
- [37]. L. Allen, M. J. Padgett, and M. Babiker. IV The Orbital Angular Momentum of Light. *Prog. Optics*, 39(1 - 3):291-372(1999).
- [38]. A. E. Siegman. *Lasers*. University Science Books, (1986).
- [39]. M. Kolobov. *Quantum Imaging*. Springer(2007).
- [40]. A. J. Gonsalves, K. Nakamura, C. Lin, D. Panasenko, S. Shiraishi, T. Sokollik, C. Benedetti, C. B. Schroeder, C. G. R. Geddes, J. van Tilborg, J. Osterhoff, E. Esarey, C. Toth, and W. P. Leemans. Tunable Laser Plasma Accelerator based on Longitudinal Density Tailoring. *Nat. Phys.* 7(11):862-866(2011).
- [41]. K. Schmid, A. Buck, C. M. S. Sears, J. M. Mikhailova, R. Tautz, D. Herrmann, M. Geissler, F. Krausz, and L. Veisz. Density-transition based electron injector for laser driven wakefield accelerators. *Phys. Rev. ST Accel. Beams* 13, 091301(2010).
- [42]. A. Buck, J. Wenz, J. Xu, K. Khrennikov, K. Schmid, M. Heigoldt, J. M. Mikhailova, M. Geissler, B. Shen, F. Krausz, S. Karsch, and L. Veisz. Shock-Front Injector for High-Quality Laser-Plasma Acceleration. *Phys. Rev. Lett.* 110, 185006(2013).
- [43]. A. A. Golovanov, I. Yu. Kostyukov, J. Thomas, and A. Pukhov. Analytic model for electromagnetic fields in the bubble regime of plasma wakefield in non-uniform plasmas. *Phys. Plasmas* 24(10)(2017).
- [44]. J. Vieira, and A. J. Mendon. Nonlinear Laser Driven Donut Wakefields for Positron and Electron Acceleration. *Phys. Rev. Lett.* 112(21): 215001(2014).
- [45]. Guo-Bo Zhang, Min Chen, C. B. Schroeder, Ji Luo, Ming Zeng, Fei-Yu Li, Lu-Le Yu, Su-Ming Weng, Yan-Yun Ma, Tong-Pu Yu, Zheng-Ming Sheng, and E. Esarey. Acceleration and evolution of a hollow electron beam in wakefields driven by a Laguerre-Gaussian laser pulse. *Phys. Plasmas* 23(3):033114(2016).
- [46]. W. Lu, M. Tzoufras, C. Joshi, F. S. Tsung, W. B. Mori, J. Vieira, R. A. Fonseca, and L. O. Silva. Generating multi-gev electron bunches using single stage laser wakefield acceleration in a 3d nonlinear regime. *Phys. Rev. ST Accel. Beams* 10, 061301 (2007).
- [47]. W. Lu, C. Huang, M. Zhou, W. B. Mori, and T. Katsouleas. Nonlinear Theory for Relativistic Plasma Wakefields in the Blowout Regime. *Phys. Rev. Lett.* 96(16):165002(2006).
- [48]. I. Kostyukov, A. Pukhov, and S. Kiselev. Phenomenological theory of laser-plasma interaction in "bubble" regime. *Phys. Plasmas* 11(11):5256-5264(2004).
- [49]. S. Y. Kalmykov, A. Beck, S. A. Yi, V. N. Khudik, M. C. Downer, E. Lefebvre, B. A. Shadwick, and D. P. Umstadter. Electron self-injection into an evolving plasma bubble: Quasi-monoenergetic laser-plasma acceleration in the blowout regime. *Phys. Plasmas* 18(5):R6189(2011).
- [50]. S. Kalmykov, S. A. Yi, V. Khudik, and G. Shvets. Electron self-injection and trapping into an evolving plasma bubble. *Phys. Rev. Lett.* 103(13):135004(2009).
- [51]. L. M. Gorbunov, S. Y. Kalmykov, and P. Mora. Laser wakefield acceleration by petawatt ultrashort laser pulses. *Phys. Plasmas* 033101 (2005).
- [52]. N. E. Andreeva, L. M. Gorbunov, P. Mora, and R. R. Ramazashvili. Filamentation of ultrashort laser pulses

propagating in tenuous plasmas. *Phys. Plasmas* 14, 083104 (2007).